On the Dimensional Control of 2D Hybrid Nanomaterials

Alessandro Longo,[a, b] Dirk-Jan Mulder,[c, d] Huub P. C. van Kuringen,[c, d] Daniel Hermida-Merino,[a] Dipanjan Banerjee,[e] Debarshi Dasgupta,[c] Irina K. Shishmanova,[c] Anne B. Spoelstra,[h] Dirk J. Broer,[c, f] Albert P. H. J. Schenning,*[c, f] and Giuseppe Portale*[g]

Abstract: Thermotropic smectic liquid crystalline polymers were used as a scaffold to create organic/inorganic hybrid layered nanomaterials. Different polymers were prepared by photopolymerizing blends of a hydrogen bonded carboxylic acid derivative and a 10% cross-linker of variable length in their liquid crystalline phase. Nanopores with dimensions close to 1 nm were generated by breaking the hydrogen bonded dimers in a high pH solution. The pores were filled with positively charged silver (Ag) ions, resulting in a layered silver(I)-polymeric hybrid material. Subsequent exposure to a $NaBH_4$ reducing solution allowed for the formation of supported hybrid metal/organic films. In the bulk of the film the dimension of the Ag nanoparticles (NPs) was regulated with subnanometer precision by the cross-linker length. Ag nanoparticles with an average size of 0.9, 1.3, and 1.8 nm were produced inside the nanopores thanks to the combined effect of spatially confined reduction and stabilization of the nanoparticles by the polymer carboxylic groups. At the same time, strong Ag migration occurred in the surface region, resulting in the formation of a nanostructured metallic top layer composed of large (10–20 nm) NPs.

Introduction

Inorganic/organic hybrid materials are currently receiving a lot of attention due to their appealing functional properties and potential applications.[1–4] In particular, the incorporation of metal nanoparticles (NPs) inside polymer matrixes has opened pathways to produce flexible composites with a broad range of novel applications.[5] Inclusion of noble metal NPs into polymers has been successfully used to produce chemical and biological sensors,[6–8] plasmonic nanostructures[9–11] and novel catalytic materials.[12–14] The properties of these hybrid materials strongly depend on the size of the nanoparticles and on their spatial distribution inside the matrix.

Metal NPs with size in the range 2–10 nm are of great interest as they show size-dependent chemical and physical properties strongly different than those from the bulk materials.[15,16] Metal NPs with very low size polydispersity can be efficiently prepared in solutions and suspensions using different methods such as digestive ripening,[17,18] seeding[19] chemical reduction in the presence of a coordinating solvent,[20] microemulsions[21] and block copolymer micelles[22,23] or dendrimers.[24] Several methods are also available to produce hybrid organic/inorganic materials with controlled NP dimensions down to 5 nm. These methods include the use of mesoporous silica,[25–27] block copolymers,[23,28–30] hydrogels,[31,32] and lyotropic liquid crystalline materials.[33–36] When the NP dimension is reduced

[a] Dr. A. Longo, Dr. D. Hermida-Merino
Netherlands Organization for Scientific Research (NWO)
European Synchrotron Radiation Facility (ESRF), DUBBLE-CRG
38043 Grenoble (France)

[b] Dr. A. Longo
CNR-ISMN, Consiglio Nazionale delle Ricerche
Istituto per lo Studio dei Materiali Nanostrutturati
Via Ugo La Malfa 153, 90146 Palermo (Italy)

[c] D.-J. Mulder, Dr. H. P. C. van Kuringen, Dr. D. Dasgupta, Dr. I. K. Shishmanova, Prof. Dr. D. J. Broer, Prof. Dr. A. P. H. J. Schenning
Department of Functional Organic Materials and Devices
Chemical Engineering and Chemistry
Eindhoven University of Technology
De Rondom 70, 5612 AP Eindhoven (The Netherlands)
E-mail: a.p.h.j.schenning@tue.nl

[d] D.-J. Mulder, Dr. H. P. C. van Kuringen
Dutch Polymer Institute (DPI)
PO Box 902, 5600 AX Eindhoven (The Netherlands)

[e] Dr. D. Banerjee
Dutch-Belgian Beamline (DUBBLE)
ESRF–The European Synchrotron, CS 40220
38043 Grenoble Cedex 9 (France)

[f] Prof. Dr. D. J. Broer, Prof. Dr. A. P. H. J. Schenning
Institute for Complex Molecular Systems
Eindhoven University of Technology
P.O. Box 513, 5600 MB Eindhoven (The Netherlands)

[g] Dr. G. Portale
Macromolecular Chemistry&New Polymeric Materials
Zernike Institute for Advanced Materials
University of Groningen, Nijenborgh 4
9747 AG Groningen (The Netherlands)
E-mail: portale@rug.nl

[h] A. B. Spoelstra
Center for Multiscale Electron Microscopy, Chemical Engineering and Chemistry
Eindhoven University of Technology, P.O. Box 513
5612 AP Eindhoven (The Netherlands)

Supporting Information for the article and ORCID identification number(s) for the author(s) of this article can be found under https://doi.org/10.1002/chem.201701493.

© 2017 The Authors. Published by Wiley-VCH Verlag GmbH & Co. KGaA. This is an open access article under the terms of Creative Commons Attribution NonCommercial License, which permits use, distribution and reproduction in any medium, provided the original work is properly cited and is not used for commercial purposes.

 © 2017 The Authors. Published by Wiley-VCH Verlag GmbH & Co. KGaA, Weinheim

below 2 nm, peculiar properties are observed because of the extremely high surface-to-volume ratio.[37] The production of hybrid materials containing such ultrasmall NPs (<2 nm) with controlled dimensions is more challenging. Most of these supported ultrasmall NPs are nowadays produced inside different type of zeolites[38] and metallo-organic frameworks.[39] The in situ production of ultrasmall NPs inside flexible nanoporous polymeric supports is less explored, although potentially interesting for catalysis and optics applications.[40–42]

Recently, we have introduced novel nanoporous thermotropic smectic liquid crystalline polymers that are promising to generate hybrid inorganic/organic films.[43,44] In this work, we exploit the use of these nanoporous liquid crystalline polymers to produce silver NPs/polymer hybrid films supported on glass. We have investigated the dimensional control in these nanomaterials in detail using a variety of techniques, including microscopy, X-ray spectroscopy and depth sensitive X-ray scattering, to determine the scope and limitation of this fabrication method.

Results and Discussion

Nanoporous smectic liquid crystalline networks with different cross-linker lengths

Firstly, we have investigated the liquid crystalline behavior of mixtures containing acrylate based benzoic acid (6OBA) hydrogen bonded dimers and different cross-linkers (10% w/w) of variable length that will be used to prepare lamellar nanoporous networks with controlled pore dimensions (Figure 1). The cross-linkers have an increasing extended molecular length of 3.4, 4.0, and 5.4 nm and will be named as C3, C6, and C11, respectively. C6 has the same length of the 6OBA dimer. It should be noted that the C6 containing nanoporous material has already been partially characterized previously.[43,45]

All the dimer/cross-linker blends show a SmA structure in the same temperature range of the pure 6OBA molecule, independently of the cross-linker length, as a result of the chemical compatibility between the cross-linker and the 6OBA molecules. When heated from ambient temperature to 120 °C, pure 6OBA undergoes a series of transitions along the path Cr-SmA-N-I (with Cr = crystalline, SmA = smectic A, N = Nematic, and I = isotropic phase) as evidenced by POM and DSC analysis (see Figure S1 and S2 and Table S1). The SmA structure can be easily deduced from WAXD images taken in the liquid crystalline phase under the magnetic field (Figure S3). The layer spacing *l* is around 4.0–4.3 nm for all the samples. The addition of 10% w/w cross-linker does not alter significantly the layer spacing of the mixtures.

A polymer network is obtained by UV-photopolymerizing the acrylate units present in the blends of 90% 6OBA dimer with 10% w/w of cross-linker at 85 °C, where all the blends are in the SmA phase. The photopolymerization process induces a molecular reorganization associated to a structural transition from the SmA phase to a smectic C (SmC) phase independently of the cross-linker used as observed by X-ray diffraction. WAXD images of the photopolymerized samples show a four-point pattern in the low angle region, revealing a SmC-like structure for all polymeric networks (Figure 2, top panels). The tilt angle between the layer normal and the molecules β_{SmC} varies between 44° and 46°. The layer spacing *l* observed for the SmC structure is systematically lower than the value observed in the SmA phase and is equal to 2.8 nm for the C3, 2.9 nm for the C6 and 3.1 nm for the C11 films. Apart the 6OBA/C6 mixture, the theoretical layer spacing *l* values calculated accordingly to the tilt angle and the cross-linker molecular length (2.4 nm for C3, 2.8 nm for C6 and 3.9 nm for C11) are different from the experimentally measured ones, suggesting

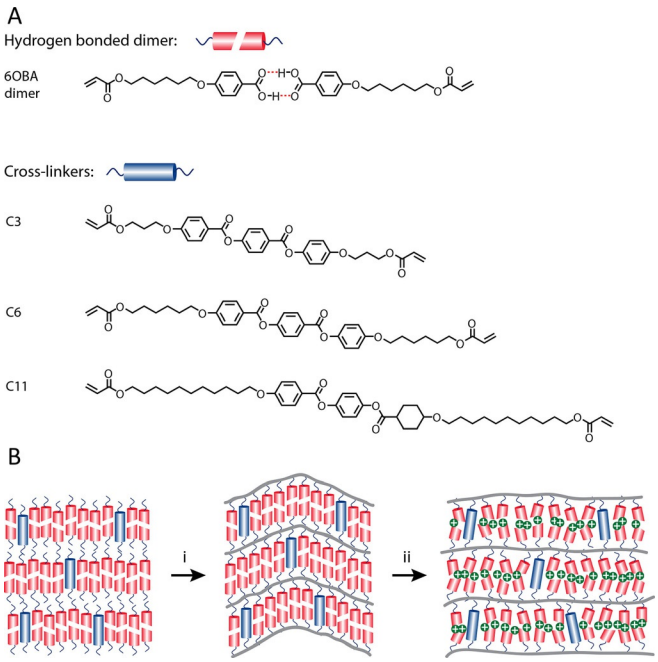

Figure 1. A) Chemical structures of the hydrogen-bonded LC dimer 6OBA and the three cross-linkers used: C3, C6, and C11. B) Schematic representation of the formation of the nanoporous smectic liquid crystalline network: i) photopolymerization in the smectic mesophase, and ii) alkaline treatment to create a nanoporous polymer film.

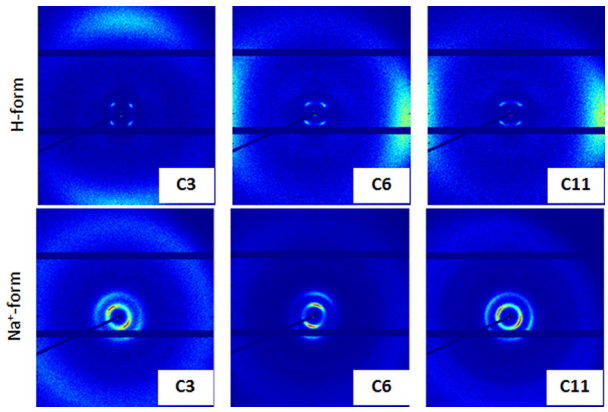

Figure 2. Top) WAXD images for the polymeric LC networks in the close-pore configuration with SmC structure. Bottom) WAXD images for the polymeric LC sodium salt networks in the open-pore configuration in the dry state.

© 2017 The Authors. Published by Wiley-VCH Verlag GmbH & Co. KGaA, Weinheim

that l is mostly determined by the 6OBA dimer length, rather than the cross-linker length.

After soaking the films in a NaOH aqueous solution, hydrogen bonds are broken.[46] The SmC structure is lost and a layered SmA structure is formed instead. X-ray images of the dry polymer salt films show clear 1st and 2nd order reflections in the low angle region, typical for a layered structure (Figure 2, bottom panels). The layer spacing l is 3.1 nm for the C3 and 3.3 nm for the C6 and C11. The signals are slightly oriented, suggesting a preferred macroscopic orientation of the layers in the polymerized samples after H-bond breaking. However, the signal at large angles is completely isotropic, revealing a disordered organization of the benzoate groups inside the layers (Figure 1 B).

The pore size can be extracted from the 1 D SAXS profiles of the nanoporous polymers in their dry state (profiles obtained from integration of the 2 D images in Figure 2 bottom panels and reported in Figure 3 A). The measured scattering intensity is proportional to the product of the form factor $|F(q)|^2$ and the structure factor $S(q)$

$$I(q) \propto |F(q)|^2 S(q) \tag{1}$$

For a 1 D lattice constituted by n electron density levels of thickness d, the scattered amplitude has the form

$$F(q) = \sum_{i=1}^{n-1} \frac{2(\rho_{i+1} - \rho_i)}{q} \sin\left(\frac{qd_i}{2}\right) \tag{2}$$

The electron density profile $\rho(z)$ can be calculated by inverse cosine Fourier transform from the scattering amplitude $F(q)$ as

$$\rho(z) = 2\int_0^\infty F(q)\cos(qz)\exp(-0.5q^2)dq \tag{3}$$

The best fit to the experimental data was obtained by using a model with three levels and a 1 D lattice with thermal disorder.[47,48] Two levels did not allow to fit the data, while using more than 3 levels did not improve the fit further. According to the electron density profiles (Figure 3 B), the pore dimension is close to 1 nm for all three materials, independently of the cross-linker length, suggesting that the pore size is not influenced by the cross-linker length in the dry state. Most of the scattering contrast arises from the electron density difference between the pores (containing cations, carboxylate groups and eventually water molecules) and the organic matrix. We found that the contrast term follows the trend C3 > C11 > C6. The introduction of a cross-linker molecule of different length than the supramolecular dimer causes an increase in electron density of the pores. The electron density of the C6 layers is the lowest, as the C6 cross-linker has the molecular structure most similar to the dimer. However, the shorter length of the C3 spacer provides a more rigid structure with well-defined layers, giving the highest scattering intensity. Unfortunately, it was not possible to determine in the same way the electron density profiles and thus the pore size in the wet membranes, as the structure of the wet membranes is sensibly more disordered than the dry one (see Figure S4).

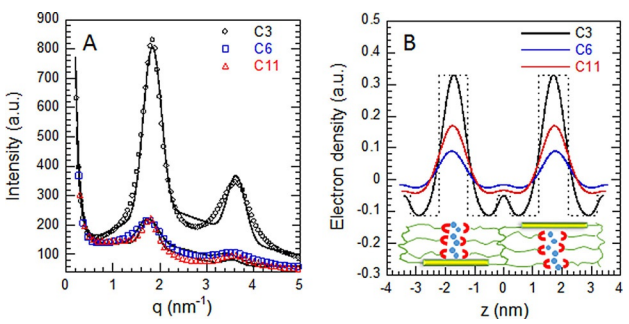

Figure 3. A) SAXS intensity for the networks in the open pore dry state (Na^+ salt form). Solid lines are best fits using [Equation (1)] with a 3 phase system. B) Calculated electron density profiles $\rho(z)$ using [Eq. (3)]. Dashed line is the ideal model with sharp interphases.

Ag^+ ion exchange and Ag nanoparticle formation

Hybrid nanomaterials supported on glass substrates were prepared by placing the 6OBA/cross-linker blends between two glass slides, the bottom one being functionalized with acrylates, in order to provide covalent binding to the glass substrate after polymerization. After UV photopolymerization, the supported films were treated with NaOH as reported above to break the H-bond and form the nanopores. The silver salt polymers were prepared according to our earlier reported procedure.[43] Na^+ ions are quantitatively exchanged with Ag^+ by submersing the membranes for 24 h in an $AgNO_3$ solution. The ion exchange is complete as confirmed by TGA and XPS analysis (see Figure S5 and S6) and the Ag^+ content inside the polymer network depends only on the stoichiometry relationship with the COO^- groups, that is, one Ag^+ for COO^- group. Extended X-ray absorption fine structure (EXAFS, Figure S7) and small-angle X-ray diffraction (SAXS, Figure S8) results after ion exchange show a more compact layer arrangement as a result of Ag-Ag bridge formation that induces dimerization of opposite carboxylate units (see structure in Figure S7 C). For instance, the layer spacing of the C11 polymer Ag^+ salt is 2.9 nm, significantly lower than the Na^+ salt form (3.4 nm).

Supported hybrid lamellar Ag NPs/polymer networks are then obtained via chemical reduction of the Ag^+/LC polymers by immersion in an aqueous $NaBH_4$ solution. Ag^+ ion reduction is quantitative as evidenced from the shift to lower energies of the EXAFS absorption edge, with final position of $E =$ 25.510 KeV, identical to standard metallic Ag (Figure S9 A). Ag^+ reduction is also confirmed by the decrease in the 3d silver binding energy in the XPS data (Figure S6 and S10). The fine structure of Ag NPs was studied by EXAFS (Table S3). The coordination of each silver atom by six to eight other silver atoms placed at a distance of ranging from 2.858 to 2.870 Å, which is close to the first shell distance in bulk *fcc* Ag, confirms the presence of silver nanoparticles and is in agreement with the known internal arrangement of silver atoms inside small clusters.[49–51] The Fourier transforms (FT) extracted from the EXAFS spectra (Figure S9 B) and reported in Figure 4 A are dominated

 © 2017 The Authors. Published by Wiley-VCH Verlag GmbH & Co. KGaA, Weinheim

by the first shell distance contribution, whose magnitude gives the average first shell coordination number.[52] For small spherical metal clusters with *fcc* structure, the average coordination number per each shell extracted from EXAFS analysis is smaller than the value observed for the corresponding bulk metal and can be used to predict the size of the clusters with great precision.[49,53,54] Using the Borowski equation,[53] the average size of the Ag NPs formed inside the C3, C6 and C11 hybrid films was calculated to be 0.9, 1.3 and 1.8 nm, respectively. Remarkably, we found that the average size of the NPs is controlled by the cross-linker length and increases nearly linear with increasing the cross-linker length (Figure 4B). The linear dependence of the nanoparticle size with the cross-linker length may appear unexpected as a similar pore size was found for the different cross-linkers in the Na^+ salt films (see Figure 3). However, it was found earlier for similar films that the degree of swelling in the smectic LC films depends on the cross-linker content.[46] Similarly, swelling of the polymer films due to water absorption is expected to take place also during the formation of the silver nanoparticles in our supported networks (see below for discussion about the network swelling), leading to pores of which the dimensions in the direction perpendicular to the layer planes are controlled by the cross-linker length. Subsequently, the pore dimension defined by the cross-linker length determines the size of the NPs in the bulk of the films.

The average number of atoms per silver cluster can be estimated using the equation $d = \left|a * (3/(2\pi))^{1/3} * n_{atoms}^{1/3}\right|$, where a is the silver cubic lattice parameter (4.0855 Å) and d is the average cluster diameter.[52,55] Consequently, silver nanoclusters with approximately 23, 70 and 185 atoms are produced inside the nanopores of the C3, C6, and C11 films, respectively. Interestingly, 13, 55, 146, 309 and 561 atoms are needed to complete one, two, three, four and five coordination shells of a *fcc* silver cluster (with cubic octahedron habit) according to the relation $n_{atoms} = (n^3*10 + n^2*15 + n*11 + 3)/3$, where n is the average number of filled shells.[55] Notably, the silver NPs produced in the bulk of the membrane and inside the nanopores of the C3, C6, and C11 networks are thus large about 1, 2 and 3 shells, respectively.

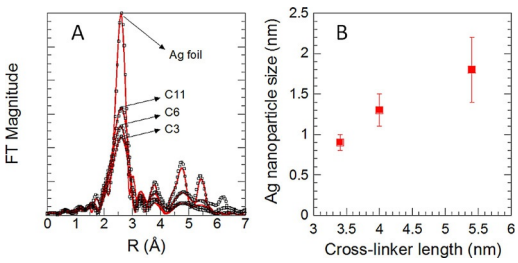

Figure 4. A) Extracted and calculated Fourier transforms for the Ag NPs LC hybrid networks. Data for standard Ag foil have been also inserted for comparison. B) Size of the Ag NPs versus the length of the cross-linker used to prepare the polymeric networks.

Information about the stabilization of such small Ag NPs inside our liquid crystalline networks can be obtained using FT-IR (Figure S11). The presence in the Ag NPs/LC polymer hybrid films of the symmetric ($v_s(COO^-)$) and antisymmetric stretching $-COO^-$ ($v_{as}(COO^-)$) bands at 1543 and 1386 cm^{-1} suggests that the interaction with the nanoparticles is via the carboxylate groups. Moreover, the $-COO^-$ scissor band located at 854 cm^{-1} is strongly enhanced in the Ag NPs/LC polymer hybrid films due to the interaction between carboxylate groups and silver atoms from the clusters. The ionic nature of the polymer/NP interaction can be inferred according to the frequency difference $\Delta v = v_{as}(COO^-) - v_s(COO^-) = 158\,cm^{-1}$[56] which is in agreement with what is reported for polyacrylates[57] and carboxylic acids.[58,59]

In order to get an insight into the mechanism of formation of these supported 2D hybrid nanomaterials, the Ag NPs/hybrid polymer containing the C11 cross-linker was further studied by TEM and depth resolved grazing-incidence small-angle scattering (GISAXS). Remarkably, cross-section TEM images recorded at increasing distances from the film surface showed a gradient in the size of the NPs along the thickness of the polymer film (Figure 5). The average dimension of the Ag NPs at the surface is about 20 nm (Figure 5B). Immediately below the surface, a dense 10 nm Ag NP layer is formed. This dense NP layer extends for few hundreds of nanometers with a rather irregular transition region. About 1 μm below the film surface, in the center of the supported film, 5 nm Ag nanoparticles are mostly observed (Figure 5C).[43] However, Ag NPs with average size of 2.7 ± 0.4 nm are observed in the bottom half region of the film, further away from the surface (Figure 5D and Figure S12A–C). This value is larger than the size determined by EXAFS for the C11 sample (1.8 nm). This difference might be due to the fact that the thinnest microtomed section we can produce is about 70 nm and the polymeric matrix is causing a noisy background, making it difficult to ob-

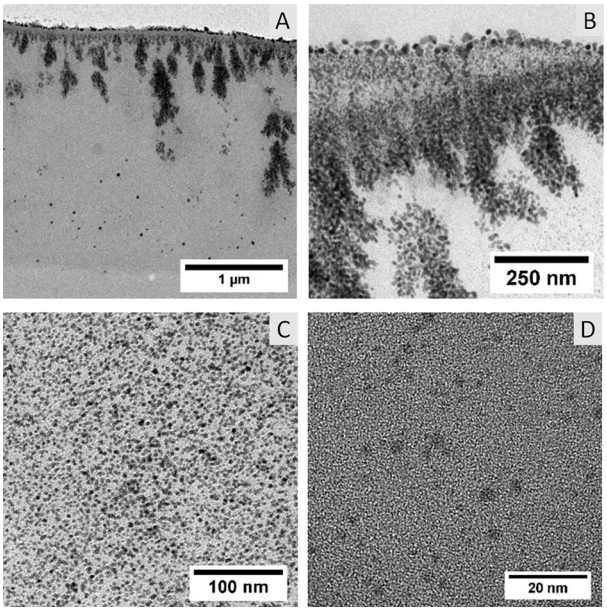

Figure 5. TEM images of the chemically reduced Ag NPs/LC polymer with C11 cross-linker supported on glass. A) View of the entire film cross section; B) of the surface region; C) of the centre of the film; D) of region close to the substrate.

© 2017 The Authors. Published by Wiley-VCH Verlag GmbH & Co. KGaA, Weinheim

serve the smaller NPs. Few sparse larger NPs (>10 nm) are present in the bottom half region and have clearly formed outside the nanopores. Interestingly, the 5 nm NPs observed by TEM have dimensions close to the molecular length of the C11 cross linker, much larger than the measured pore dimension. However, NPs with size similar to the cross-linker length have not been observed inside the Ag/C6 networks (Figure S13), where only NPs of about 1 nm are observed inside the film. The 5 nm NPs might thus be the result of a further growth of the smaller 2 nm ones in the more flexible highly swollen C11 network. However, the total amount of NPs larger than 2.7 nm must be negligible, as during the EXAFS measurements X-rays cross the whole film and gather information about the bulk structure of the film.

The hybrid nanomaterial with the C11 cross-linker was also characterized by GISAXS which is a depth sensitive technique and provides structural information from 1 to 100 nm.[60–64] Increasing gradually the X-ray angle of incidence α_i with respect to the sample surface allows higher penetration inside the film, giving the possibility to measure the size of the nanoparticles at different penetration depths. A typical GISAXS image recorded at $\alpha_i = 0.25^\circ$ reveals at high scattering angles two signals related to the 1st and 2nd order of the layered SmA LC polymeric network structure (Figure S14). The intensity of these two signals is regrouped in the vertical direction, suggesting that these hybrid materials form a 2D layered structure with an average orientation of the layers parallel to the glass substrate, in agreement with the layered structure observed by AFM for similar films.[43] The layer spacing is about 4 nm, significantly higher than the value measured for the Ag^+-salt form, as the nanopores now contain Ag NPs. The GISAXS intensity scattered at low angles along the parallel q_y direction provides quantitative information about the nanoparticle lateral dimensions (Figure 6A). For all the samples, a strong intensity upturn at low q_y values is recorded for $\alpha_i < 0.2^\circ$, suggesting that the signal is dominated by scattering from the larger Ag NPs located at the film surface (already observed by TEM in Figure 5A).[65,66] For $\alpha_i > 0.2^\circ$, the intensity upturn decreases and the intensity at low q_y becomes flat in the log-log plot for $\alpha_i \gg \alpha_c$ of silver (where $\alpha_c = 0.3^\circ$ is the critical angle for bulk silver), suggesting that the contribution from the nanostructures present on the surface becomes negligible with respect to the structures inside the network. Furthermore, the scattering intensity shifts to higher q_y values, indicating that smaller nanoparticles are observed at the higher incident angles (i.e. higher penetration depth). No diffraction peaks are detected along q_y suggesting the absence of positional ordering and/or significant aggregation between the nanoparticles inside the network. In order to highlight the differences among the GISAXS scattering profiles acquired at different incident angles we have used the so-called Kratky plot (see Figure 6B). The $I(q_y)*q_y^2$ versus q_y curve in the Kratky plot for $\alpha_i = 0.2^\circ$ clearly shows two Ag NPs populations with different average size. Simulation of the GISAXS images provides information about the nanoparticle size and shape. GISAXS images can be successfully simulated by an ensemble of polydisperse spheroidal Ag NPs. Simulation of the GISAXS image recorded at $\alpha_i = 0.2^\circ$ reveals two populations of Ag NPs with average size of 11 and 5 nm and relative abundance of 16% and 84%, respectively (see Figure S15). For $\alpha_i = 1.1^\circ$, GISAXS simulations yield an average lateral dimension of 4.6±0.4 nm in agreement with TEM images reported in Figure 5C and with previously reported data.[43] Unfortunately, the small 2–2.5 nm NPs observed by TEM and EXAFS are not observed by GISAXS as they scatter far less and the GISAXS intensity scales with the volume squared of the objects.

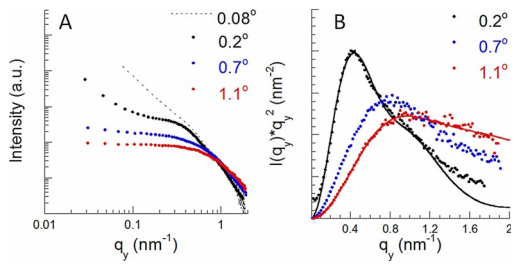

Figure 6. GISAXS results for the hybrid Ag NPs/C11 film. A) Parallel GISAXS intensity as a function of increasing incident angle. B) Kratky plot for the parallel $I(q_y)$ GISAXS intensity. Solid lines are the best fits obtained using the Is-GISAXS software.

The formation of Ag NPs inside the supported LC polymeric networks and the gradient in size of the NPs along the film thickness generated by the chemical reduction and revealed by TEM and depth-sensitive GISAXS can be explained on the basis of some considerations about the network swelling behavior. Previously, it has been observed for the free-standing films using C6 cross-linker that swelling predominantly occurs in the direction parallel to the smectic layers whilst only limited swelling was observed in the perpendicular direction (Figure S16).[46] In our case, the polymer is covalently linked to the glass substrate resulting in an asymmetric lateral swelling in the direction perpendicular to the substrate that generates vertical pathways for the diffusion of the reducing solution. The network density increases going from the polymer/solution to the polymer/substrate interface, which results in a more efficient control of the size of the NPs in the lower half part of the supported networks. Larger nanoparticles are formed in the region close to the surface due to severe swelling, fast Ag migration and nanoparticle aggregation. Slow diffusion inside the layers in the bulk of the film and far from the surface allows for the formation of small Ag NPs with controlled size and limited polydispersity (Figure 7). The severe swelling experienced during reduction by the top part of the film causes an extra porosity that extends in the vertical direction and can be responsible for the formation of the branched structures observed in Figure 6A.

Conclusion

Nanoporous liquid crystalline smectic networks having cross-linkers with increasing molecular length have been used to obtain liquid crystalline polymer/silver nanoparticle hybrid materials. The formation process of nanoparticles inside the films has been elucidated using state-of-the-art characterization

© 2017 The Authors. Published by Wiley-VCH Verlag GmbH & Co. KGaA, Weinheim

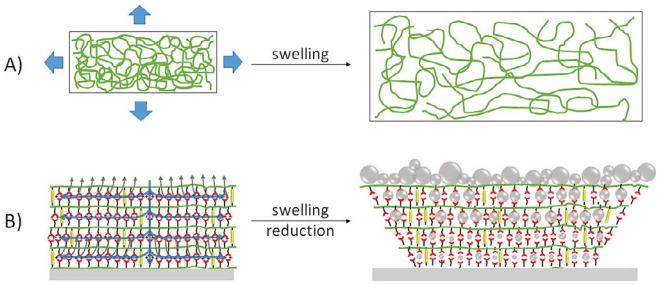

Figure 7. A) Top view of the strong lateral swelling of the networks containing the C11 cross-linker. Chain density decreases drastically in the network regions close to the surface. B) Scheme for the process of nanoparticle formation inside supported LC lamellar networks. Diffusion of the reducing solution inside the network is depicted by the blue arrows. Migration and aggregation of Ag NPs at the solution/polymer interface are highlighted by grey arrows.

techniques. Ultrasmall silver nanoparticles with dimensions ranging from 0.9 to 1.8 nm are formed inside the polymer nanopores. The formation of such ultrasmall nanoparticles is possible thanks to the spatially confined silver ion reduction within the nanopores and to the ionic stabilization of the nanoparticles by the carboxylic groups contained in the pores. The subnanometer control is however restricted to the bulk of the film, away from the film surface where severe network swelling occurs.

Our results clearly suggest that controlling the swelling of these supported nanoporous materials, by for instance increasing the amount of cross-linker molecules,[45] might be the key to obtain monodisperse nanoparticles of controlled size through the whole film. Therefore, the use of nanoporous liquid crystalline smectic network could represent an attractive method to prepare hybrid materials where the size of the nanoparticles can be controlled with subnanometer precision down to 1 nm.

The synthetic approach is not limited to silver particles, but can in principle also be applied to other metal particles. Our detailed multiscale characterization provides guidelines for the design of hybrid nanomaterials with controlled hierarchical dimensions and programmed functional properties such as tailored surface conductivity, specific catalytic activity, reflectivity and graded refractive index materials.

Experimental Section

Fabrication of the hybrid nanostructured materials

Homeotropically aligned smectic networks were produced by processing the liquid crystalline (LC) mixtures in the nematic phase at 105 °C by capillary suction between two accurately 6 μm spaced glass plates. These glass plates (30×30 mm) were cleaned prior to use with ethanol in an ultrasonic bath for 20 minutes, blow-dried with N_2 and exposed to UV ozone treatment for 20 minutes. One glass plate was then functionalized with 3-methacryloxypropyltrimethoxysilane. A functionalized and a non-coated glass plates were glued together with glue containing 6 μm sized spacers. The filled LC cells were cooled to the smectic A phase at 85 °C and exposed to a UV light using a mercury lamp (OmniCure S1000) that emitted at 365 nm with an intensity of approximately 5 mW cm^{-2} at the sample surface. The samples were illuminated for 5 minutes, followed by an additional heat treatment at 120 °C to ensure maximum conversion of the acrylate groups. The non-coated glass plate was then removed, generating a glass plate coated with a 6 μm thick covalently attached homeotropic smectic polymer network. In order to produce Ag^+-networks, the smectic networks were exposed to 0.05 M NaOH solution for 1 h, washed with distilled water and subsequently treated with 0.2 M $AgNO_3$ solution for 24 h and washed again with distilled water, while covered with aluminium foil. Chemical reduction was performed using a 0.2 M $NaBH_4$ aqueous solution for approximately 30 minutes. The resulting inorganic/organic hybrid film was subsequently rinsed with water and dried at ambient humidity.

Transmission electron microscopy (TEM)

For transmission electron microscopy the polymer films were embedded in an EPOFIX epoxy resin media. Cross sections were cut at room temperature using an ultra-microtome (Reichert-Jung Ultracut E) with 60–70 nm setting thickness. The obtained cross sections were transferred to a carbon film containing 400 square mesh copper grids. The imaging was performed on a Tecnai G2 Sphera by FEI operated in bright-field mode at 300 kV under slight underfocus conditions.

Extended X-ray absorption fine structure (EXAFS)

Ag K-edge (25.510 KeV) EXAFS spectra were collected at the Dutch-Belgian Beam Line (BM26A-DUBBLE) at the European Synchrotron Radiation Facility (ESRF).[67] The energy of the X-ray beam was tuned by a double-crystal monochromator operating in fixed-exit mode using a Si (111) crystal pair. The samples were measured in a closed-cycle He-cryostat (Oxford Instruments) at 80 K to minimize the noise induced by the thermal Debye-Waller factor. EXAFS spectra were collected in fluorescence mode using a 9-element Ge detector (Ortec Inc.), whereas reference spectra of the metallic Ag foil were collected at liquid nitrogen in transmission mode using Ar/He-filled ionization chambers. The EXAFS spectra were energy-calibrated, averaged and further analysed using GNXAS (the details about data analysis are reported in the SI file).[68,69]

X-ray diffraction (XRD)

X-ray scattering measurements of planar aligned LC polymer films were performed on a Ganesha lab instrument equipped with a GeniX-Cu ultra-low divergence source producing X-ray photons with a wavelength of 1.54 Å and a flux of 1×10^8 ph s^{-}. Scattering patterns were collected using a Pilatus 300 K silicon pixel detector with 487×619 pixels of 172 μm^2 in size placed at a sample-to detector distance of 1080 mm. From the obtained diffraction patterns azimuthal integration was performed to calculate the intensity against the scattering vector q, where $q=(4\pi/\lambda)\sin\vartheta$ (ϑ is the angle of incidence and λ is the wavelength). The beam centre and the q range were calibrated using a standard silver behenate powder as reference.

Grazing-incidence small-angle scattering (GISAXS)

Variable angle GISAXS measurements were performed at the BM26B-DUBBLE beam line at the ESRF.[70,71] An X-ray wavelength of $\lambda=0.1$ nm was used with 2 m and 4 m sample-to-detector distances. GISAXS images were recorded using a high sensitive solid state silicon photon counting Pilatus 1 M detector with pixel size of

© 2017 The Authors. Published by Wiley-VCH Verlag GmbH & Co. KGaA, Weinheim

172×172 μm and active surface dimension of 179×169 cm. The scattering angle scale 2θ was calibrated using the position of diffraction rings from a silver behenate standard powder. Direct and reflected beam positions were measured directly on the detector using a 2 mm Al filter to reduce the direct beam intensity and avoid detector damage. The nominal incident angles α_i were accurately recalibrated using the measured reflected beam position and the known sample-to-detector distance. Different angles of incidence α_i ranging from 0.08° to 1.1° were used in order to allow increased penetration depth of the supported networks. Background scattering from air was subtracted to every image before further analysis. Scattering from glass substrate was not subtracted as it contributes much less than the sample to the experimentally measured GISAXS intensity. GISAXS images were reported as a function of α_f and $2\theta_f$ angles, where α_f is the exit angle in the vertical direction and $2\theta_f$ is the in-plane scattering angle, in agreement with standard GISAXS notation.[60] Intensity cuts along the q_y direction were performed using a Matlab routine, where $q_y = 2\pi = \sin(2\theta_f)\cos(\alpha_f)]/\lambda$.

Acknowledgements

This work was supported by the Netherlands Organization for Chemical Research (CW) with financial aid from The Netherlands Organization for Scientific Research (NWO), Dutch Polymer Institute (DPI), projects 742&776 and the European Community within the Marie Curie program of Framework 7 (Hierarchy Project). NWO is also acknowledged for providing beamtime at the ESRF.

Conflict of interest

The authors declare no conflict of interest.

Keywords: liquid crystals · nanoparticles · nanoporous polymers · polymers · supported hybrid networks

[1] L. Nicole, L. Rozes, C. Sanchez, *Adv. Mater.* **2010**, *22*, 3208.
[2] A. Thawari, C. P. Rao, *ACS Appl. Mater. Interfaces* **2016**, *8*, 10392–10402.
[3] C. He, D. Liu, W. Lin, *Chem. Rev.* **2015**, *115*, 11079.
[4] K. Gregorczyk, M. Knez, *Prog. Mater. Sci.* **2016**, *75*, 1.
[5] V. M. Rotello, *Nanoparticles: Building Blocks for Nanotechnology*, Springer Science & Business Media, New York, NY, **2004**.
[6] J. Matsui, K. Akamatsu, S. Nishiguchi, D. Miyoshi, H. Nawafune, K. Tamaki, N. Sugimoto, *Anal. Chem.* **2004**, *76*, 1310.
[7] F. P. Zamborini, M. C. Leopold, J. F. Hicks, P. J. Kulesza, M. A. Malik, R. W. Murray, *J. Am. Chem. Soc.* **2002**, *124*, 8958.
[8] J. E. Kim, J. H. Choi, M. Colas, D. H. Kim, H. Lee, *Biosens. Bioelectron.* **2016**, *80*, 543.
[9] A. Biswas, O. C. Aktas, J. Kanzow, U. Saeed, T. Strunskus, V. Zaporojtchenko, F. Faupel, *Mater. Lett.* **2004**, *58*, 1530.
[10] K. M. Mayer, J. H. Hafner, *Chem. Rev.* **2011**, *111*, 3828.
[11] H. A. Atwater, A. Polman, *Nat. Mater.* **2010**, *9*, 205.
[12] M. Králik, A. Biffis, *J. Mol. Catal. A* **2001**, *177*, 113.
[13] E. Groppo, G. Agostini, E. Borfecchia, L. Wei, F. Giannici, G. Portale, A. Longo, C. Lamberti, *J. Phys. Chem. C* **2014**, *118*, 8406.
[14] E. Groppo, G. Agostini, E. Borfecchia, A. Lazzarini, W. Liu, C. Lamberti, F. Giannici, G. Portale, A. Longo, *ChemCatChem* **2015**, *7*, 2188.
[15] Cb. Murray, D. J. Norris, M. G. Bawendi, *J. Am. Chem. Soc.* **1993**, *115*, 8706.
[16] A. P. Alivisatos, *Science* **1996**, *271*, 933.
[17] B. L. V. Prasad, S. I. Stoeva, C. M. Sorensen, K. J. Klabunde, *Chem. Mater.* **2003**, *15*, 935.
[18] R. Shankar, B. B. Wu, T. P. Bigioni, *J. Phys. Chem. C* **2010**, *114*, 15916.
[19] N. R. Jana, L. Gearheart, C. J. Murphy, *Langmuir* **2001**, *17*, 6782.
[20] A. Desireddy, B. E. Conn, J. Guo, B. Yoon, R. N. Barnett, B. M. Monahan, K. Kirschbaum, W. P. Griffith, R. L. Whetten, U. Landman, T. F. Bigioni, *Nature* **2013**, *501*, 399.
[21] J. Eastoe, M. J. Hollamby, L. Hudson, *Adv. Colloid Interface Sci.* **2006**, *128*, 5.
[22] M. Antonietti, E. Wenz, L. Bronstein, M. Seregina, *Adv. Mater.* **1995**, *7*, 1000.
[23] T. Sakai, P. Alexandridis, *Langmuir* **2004**, *20*, 8426.
[24] K. Esumi, *Dendrimers for Nanoparticle Synthesis and Dispersion Stabilization in Colloid. Chem. II in Top Curr. Chem.*, Springer, Berlin, Heidelberg, **2003**, pp. 31–52.
[25] A. Fukuoka, H. Araki, Y. Sakamoto, N. Sugimoto, H. Tsukada, Y. Kumai, Y. Akimoto, M. Ichikawa, *Nano Lett.* **2002**, *2*, 793.
[26] V. Hornebecq, M. Antonietti, T. Cardinal, M. Treguer-Delapierre, *Chem. Mater.* **2003**, *15*, 1993.
[27] Z. Kónya, V. F. Puntes, I. Kiricsi, J. Zhu, P. Alivisatos, G. A. Somorjai, *Catal. Lett.* **2002**, *81*, 137.
[28] I. W. Hamley, *Nanotechnology* **2003**, *14*, R39.
[29] L. Qi, H. Cölfen, M. Antonietti, *Nano Lett.* **2001**, *1*, 61.
[30] T. N. Hoheisel, K. Hur, U. B. Wiesner, *Prog. Polym. Sci.* **2015**, *40*, 3.
[31] N. Singh, L. A. Lyon, *Chem. Mater.* **2007**, *19*, 719.
[32] E. Pavlopoulou, G. Portale, K. E. Christodoulakis, M. Vamvakaki, W. Bras, S. H. Anastasiadis, *Macromolecules* **2010**, *43*, 9828.
[33] J. H. Ding, D. L. Gin, *Chem. Mater.* **2000**, *12*, 22.
[34] T. M. Dellinger, P. V. Braun, *Chem. Mater.* **2004**, *16*, 2201.
[35] T. Hegmann, H. Qi, V. M. Marx, *J. Inorg. Organomet. Polym. Mater.* **2007**, *17*, 483.
[36] S. Saliba, C. Mingotaud, M. L. Kahn, J.-D. Marty, *Nanoscale* **2013**, *5*, 6641.
[37] J. P. Wilcoxon, B. L. Abrams, *Chem. Soc. Rev.* **2006**, *35*, 1162.
[38] N. Wang, Q. Sun, R. Bai, X. Li, G. Guo, J. Yu, *J. Am. Chem. Soc.* **2016**, *138*, 7484.
[39] C. Zlotea, R. Campesi, F. Cuevas, E. Leroy, P. Dibandjo, C. Volkringer, T. Loiseau, G. Férey, M. Latroche, *J. Am. Chem. Soc.* **2010**, *132*, 2991.
[40] A. M. Hodges, M. Linton, A.-H. Mau, K. J. Cavell, J. A. Hey, A. J. Seen, *Appl. Organomet. Chem.* **1990**, *4*, 465.
[41] D. Fritsch, K.-V. Peinemann, *J. Membr. Sci.* **1995**, *99*, 29.
[42] D. Fritsch, K.-V. Peinemann, *Catal. Today* **1995**, *25*, 277.
[43] D. Dasgupta, I. K. Shishmanova, A. Ruiz-Carretero, K. Lu, M. Verhoeven, H. P. van Kuringen, G. Portale, P. Leclère, C. W. Bastiaansen, D. J. Broer, A. P. H. J. Schenning, *J. Am. Chem. Soc.* **2013**, *135*, 10922.
[44] Y. Xu, H. P. van Kuringen, D. J. Mulder, A. P. Schenning, N. A. Sommerdijk, *RSC Adv.* **2016**, *6*, 13953.
[45] H. P. van Kuringen, G. M. Eikelboom, I. K. Shishmanova, D. J. Broer, A. P. Schenning, *Adv. Funct. Mater.* **2014**, *24*, 5045.
[46] I. K. Shishmanova, C. W. Bastiaansen, A. P. Schenning, D. J. Broer, *Chem. Commun.* **2012**, *48*, 4555.
[47] R. Hosemann, S. N. Bagchi, *Direct Analysis of Diffraction by Matter*, North-Holland Pub. Co., Amsterdam, **1962**.
[48] G. Pabst, R. Koschuch, B. Pozo-Navas, M. Rappolt, K. Lohner, P. Laggner, *J. Appl. Crystallogr.* **2003**, *36*, 1378.
[49] P. A. Montano, J. Zhao, M. Ramanathan, G. K. Shenoy, W. Schulze, J. Urban, *Chem. Phys. Lett.* **1989**, *164*, 126.
[50] G. Battaglin, E. Cattaruzza, F. Gonella, R. Polloni, F. D'Acapito, S. Colonna, G. Mattei, C. Maurizio, P. Mazzoldi, S. Padovani, C. Sada, A. Quaranta, *Nucl. Instrum. Methods Phys. Res. Sect. B* **2003**, *200*, 185.
[51] T. Yamamoto, S. Takenaka, T. Tanaka, T. Baba, *J. Phys. Conf. Ser.* **2009**, *190*, 012171.
[52] A. Longo, A. Martorana, *J. Appl. Crystallogr.* **2008**, *41*, 446.
[53] M. Borowski, *J. Phys. IV* **1997**, *7*, C2–259.
[54] A. I. Frenkel, *J. Synchrotron Radiat.* **1999**, *6*, 293.
[55] A. Cervellino, C. Giannini, A. Guagliardi, *J. Appl. Crystallogr.* **2003**, *36*, 1148.
[56] C. Ohe, H. Ando, N. Sato, Y. Urai, M. Yamamoto, K. Itoh, *J. Phys. Chem. B* **1999**, *103*, 435.
[57] J. Petroski, M. A. El-Sayed, *J. Phys. Chem. A* **2003**, *107*, 8371.
[58] S. J. Lee, S. W. Han, H. J. Choi, K. Kim, *J. Phys. Chem. B* **2002**, *106*, 2892.

 © 2017 The Authors. Published by Wiley-VCH Verlag GmbH & Co. KGaA, Weinheim

[59] K. J. Lee, Y.-I. Lee, I.-K. Shim, J. Joung, Y. S. Oh, *J. Colloid Interface Sci.* **2006**, *304*, 92.
[60] G. Renaud, R. Lazzari, F. Leroy, *Surf. Sci. Rep.* **2009**, *64*, 255.
[61] D.-M. Smilgies, P. Busch, C. M. Papadakis, D. Posselt, *J. Synchrotron Radiat.* **2002**, *15*, 35.
[62] P. Müller-Buschbaum, *Anal. Bioanal. Chem.* **2003**, *376*, 3.
[63] M. L. Chabinyc, *Polym. Rev.* **2008**, *48*, 463.
[64] P. Müller-Buschbaum, *Polym. J.* **2013**, *45*, 34.
[65] S. Lenz, M. Bonini, S. K. Nett, M. C. Lechmann, S. G. J. Emmerling, R. S. Kappes, M. Memesa, A. Timmann, S. V. Roth, J. S. Gutmann, *Eur. Phys. J. Appl. Phys.* **2010**, *51*, 10601.
[66] G. Portale, L. Sciortino, C. Albonetti, F. Giannici, A. Martorana, W. Bras, F. Biscarini, A. Longo, *Phys. Chem. Chem. Phys.* **2014**, *16*, 6649.
[67] S. Nikitenko, A. M. Beale, A. M. van der Eerden, S. D. Jacques, O. Leynaud, M. G. O'Brien, D. Detollenaere, R. Kaptein, B. M. Weckhuysen, W. Bras, *J. Synchrotron Radiat.* **2008**, *15*, 632.
[68] A. Filipponi, A. Di Cicco, *Phys. Rev. B* **1995**, *52*, 15135.
[69] A. Filipponi, A. Di Cicco, C. R. Natoli, *Phys. Rev. B* **1995**, *52*, 15122.
[70] W. Bras, I. P. Dolbnya, D. Detollenaere, R. van Tol, M. Malfois, G. N. Greaves, A. J. Ryan, E. Heeley, *J. Appl. Crystallogr.* **2003**, *36*, 791.
[71] G. Portale, D. Cavallo, G. C. Alfonso, D. Hermida-Merino, M. van Drongelen, L. Balzano, G. W. M. Peters, J. G. P. Goossens, W. Bras, *J. Appl. Crystallogr.* **2013**, *46*, 1681.

Manuscript received: April 4, 2017
Accepted manuscript online: July 13, 2017
Version of record online: August 15, 2017

 © 2017 The Authors. Published by Wiley-VCH Verlag GmbH & Co. KGaA, Weinheim